6-2

TCAD Incorporation of Physical Framework to Model N and P BTI in MOSFETs

Ravi Tiwari, Nilotpal Choudhury, Tarun Samadder, Subhadeep Mukhopadhyay, Narendra Parihar and Souvik Mahapatra

Department of Electrical Engineering, Indian Institute of Technology Bombay, Mumbai 400076, India

*Phone: +91-222-572-0408, Email: souvik@ee.iitb.ac.in

Abstract: **Negative and Positive Bias Temperature Instabilities (NBTI, PBTI) respectively in P and N channel High-K Metal Gate (HKMG) MOSFETs are modeled by trap generation (TG) and charge trapping (CT) and validated against measured data. The mechanism of TG (interface) is incorporated into TCAD and is separately validated using independent experiments. BTI kinetics is modeled at different stress bias (V_G) and temperature (T). Impacts of Nitrogen (N%) and Equivalent Oxide Thickness (EOT) scaling on the magnitude of BTI and its time, V_G and T dependencies are modeled**.

Keywords: ***threshold voltage shift, DCIV, NBTI, PBTI, EOT scaling, HKMG-MOSFETs, Nitrogen impact***

I. INTRODUCTION

Bias Temperature Instability (BTI) is a crucial reliability issue in P and N channel HKMG MOSFETs [1]. It causes shift in several device parameters such as threshold voltage (ΔV_T), linear (ΔI_{DLIN}) and saturation (ΔI_{DSAT}) drain current, subthreshold slope (ΔSS) and transconductance (Δg_m) etc. over time, due to the buildup of positive charges in the gate insulator of the transistor. These parameters recover partially when the stress is lowered or removed, resulting in lower degradation during AC as compared to DC stress. The BTI mechanism is debated and various models are proposed [2]-[4]. It is now believed that ΔV_T during NBTI in P MOSFETs is due to TG at the channel/interlayer (IL) interface (ΔV_{IT-IL}) and IL bulk (ΔV_{OT-IL}), and CT (hole, ΔV_{HT-IL}) in IL bulk, and ΔV_T during PBTI in N MOSFETs is due to the TG at IL/HK interface (ΔV_{IT-HK}) and HK bulk (ΔV_{OT-HK}), and CT (electron, ΔV_{ET-HK}) in HK bulk, see Fig.1 [1]. The BTI Analysis Tool (BAT) utilizes the uncorrelated contributions from the above subcomponents of overall ΔV_T, Fig.2, and can model the ΔV_T kinetics during DC and AC stress and recovery, as V_G, T, pulse duty cycle and frequency are varied for PBTI [5] and NBTI [6], [7], and various process changes for NBTI [7]. BAT uses double interface Reaction-Diffusion Model (RDM) for interfacial TG (density ΔN_{IT-IL} or ΔN_{IT-HK}), their charged state and contribution (ΔV_{IT-IL} or ΔV_{IT-HK}) by the Transient Trap Occupancy Model (TTOM) and empirical models for CT and bulk TG. Recently, the Activated Barrier Double Well Thermionic Model (ABDWTM) is used for hole CT for NBTI [8]. The interfacial TG kinetics during NBTI has been modeled using TCAD and validated using Direct-Current I-V (DCIV) data [12], [13]. The TCAD-NBTI framework utilizes Capture-Emission Depassivation Model (CEDM), Fig.3, and Multi-State Configuration Model (MSCM), Fig.4 to calculate TG kinetics. The framework is validated using FinFETs with different channel materials, see [9] for further details.

II. SCOPE OF WORK

PBTI interfacial trap generation is incorporated in TCAD and validated using DCIV. Although experiments suggest TG at the channel/interlayer and interlayer/High-K respectively for N and P BTI [1], due to the absence of coupling between non-local tunneling and CEDM at present, TG is calculated at the channel/IL interface for both cases, but generated traps are assigned at the IL/High-K interface to obtain ΔV_T during PBTI. TG kinetics measured using DCIV method at various V_G and T, in N and P HKMG MOSFETs having different N% and IL thickness (data from [9]) is modeled by TCAD. ΔV_T time kinetics measured using ultra-fast I-V method for the same devices [5], [6] is modeled using BAT, with the underlying interfacial TG component validated using TCAD. Impact of N% induced IL scaling (leading to EOT scaling) is modeled.

III. BTI MECHANISM

Inversion layer holes tunnel to Hydrogen (H) passivated defect precursors at the channel/IL interface at V_G<0V stress, react, break (=ΔN_{IT-IL}) and release H, Fig.3. The released H atoms diffuse and react with other H passivated defects inside IL (HK) bulk to form H_2, which diffuses away, Fig.4. This is RDM for NBTI. Interfacial TG (from DCIV) shows similar power low time kinetics for both and N and P BTI [1]. A similar process as RDM for NBTI is used for PBTI at V_G>0V stress, with inversion electrons induced dissociation of the defect precursors at the IL/HK interface (=ΔN_{IT-HK}), H atoms diffusion and defect generation at the HK bulk, and diffusion of H_2 (Figs.3 and 4), which is RDM for PBTI. The chemical nature of defects is likely different for the interfacial TG in N and P BTI. ΔN_{IT-HK} can be created directly by electrons, or by the Anode Hole Injection (AHI [11]) process, *i.e.*, tunneling of electrons from cathode to anode, impact ionization and injection of energetic hole into gate oxide, although a direct link (the former) is used in TCAD at present. Moreover, the tunneling and trapping of holes (IL) and electrons (HK) result in CT, and AHI process is also responsible for bulk TG, and these effects are handled separately in BAT.

IV. TCAD FRAMEWORK

Two-dimensional P and N channel HKMG-MOSFET device structures are generated using process simulation [12]. In device simulation [13], defect dissociation by holes (NBTI) and electrons (PBTI) is handled using CEDM-MSC framework. Only four CEDM model parameters, *i.e.*, the pre-factor (K_{F10}), temperature activation (E_{AKF}), temperature (T) independent field acceleration (Γ_0) and bond polarization (α),

Fig.3, are related to bond dissociation, and are varied to model different IL based devices used in this work. MSCM is used for diffusion of released H after bond dissociation using CEDM, dimerization into H_2 molecule assisted by reaction with another H passivated defect (at IL/High-K interface) and H_2 diffusion. All MSCM parameters are consistent between studied devices for N & P BTI. Backend of 1μm is used to allow H_2 diffusion in both BTI (length depends on stress time and T that determine the distance of H_2 diffusion).

V. DEVICE AND MEASUREMENT DETAILS

Gate First (GF) N and P HKMG MOSFETs having ultra-thin thermal IL and HfO_2 HK are used [1]. IL scaling is done using thermal process tweak for D1 (5Å) and D2 (3Å), with N% in D_2 for D3 (2.5Å) and N based IL, D4 (1.5Å), EOT of HK is 4.6Å. DCIV measured data in Figs.5-8 and Figs.12-15 are with delay correction [11], and in Figs.12-15 with (also) bandgap correction (ΔV_{IT}=K.ΔN_{IT}) [2]. ΔV_T in Figs.9-14 are measured with 10μs delay [5], [6].

VI. TCAD MODELING

Modeling of DCIV measured ΔN_{IT} time kinetics at various V_G and T are shown for N, P BTI, for devices having various N% and IL, in Figs.5 and 6. Only longer time (t>10s) data are available as DCIV is a slow method. Power law time kinetics is observed with n~1/6 for all cases (after delay correction), the slope is determined by H_2 diffusion and suggests similar process for the time kinetics in N, P BTI. Model accuracy is verified using data at different V_G x T, Fig.7. ΔN_{IT} increases for NBTI but reduces for PBTI as N% is increased, Figs.5, 6, 8, due to their different origin. The Voltage Acceleration Factor (VAF, slopes in Fig.8) reduces at higher N% for both N and P BTI.

VII. BTI MODELING

Measured and modeled ΔV_T kinetics are shown for N and P BTI, Figs.9, 10. The underlying subcomponents (ΔV_{IT} from RDM, ΔV_{HT} and ΔV_{ET} from ABDWTM) are shown at fixed V_G, T, Fig.9. Interface TG dominates ΔV_T for both N, P BTI at longer time (t>1s) and shows power-law time dependence with slope of n~1/6, due to H_2 diffusion in RDM as discussed before. DCIV calibrated TCAD with a fixed correction factor K is used for difference in scanned bandgap between DCIV and V_T measurements [2]. Bulk TG also has power-law time dependence with long-time slope n~1/3. CT saturates at long time (n~0 in a log-log plot). The model is validated across different V_G and T, Fig.10, 11 (only few examples are shown, the validation is done for other stress conditions as well).

VIII. EOT SCALING

Modeling of measured overall ΔV_T (from ultra-fast I-V) and ΔV_{IT} (from DCIV) versus EOT is shown in Fig.12. Time slope n, Fig.13, T activation energy (E_A), Fig.14 and VAF, Fig.15 versus EOT (~IL scaling) of ΔV_T and ΔV_{IT} are shown for N and P BTI. ΔV_{IT} dominates ΔV_T, both for NBTI and PBTI, in these experiments. There is a slight reduction in PBTI degradation at scaled EOT (due to Nitridation). This is consistent with higher N% resulting in higher ΔV_{IT-IL} and lower ΔV_{IT-HK} (from calibrated TCAD), lower ΔV_{OT-IL} and ΔV_{OT-HK}, and higher pre-existing trap density (it is verified by 1/f noise measurements in [1]). Since CT saturates, n of ΔV_T reduces at lower EOT (more reduction than n of ΔV_{IT}), Figs.13. Since CT has lower E_A than TG [5]-[8], E_A of ΔV_T reduces (more reduction than ΔV_{IT}) at lower EOT due to Nitridation (D3). VAF for ΔV_{IT} hence ΔV_T reduces for both BTI as IL is scaled (as ΔV_{IT} dominates ΔV_T), Fig.15.

IX. CONCLUSION

TCAD is enabled for interface TG during BTI in N and P channel MOSFETs. BAT with RDM for interface TG (same as TCAD) and ABDWTM for CT is used to model N and P BTI in differently processed MOSFETs. TCAD and BAT are separately validated with measured BTI data from differently processed devices. Further work is underway to incorporate a Reaction Drift Diffusion Model (RDDM) for bulk TG and ABDWT for CT for complete BTI solution using TCAD.

REFERENCES

[1] K. Joshi *et al.*, "HKMG process impact on N, P BTI: Role of thermal IL scaling, IL/HK integration and post HK nitridation," in *Proc. IEEE Int. Rel. Phys. Symp. (IRPS)*, Apr. 2013, pp. 4C.2.1–4C.2.10. doi: 10.1109/IRPS.2013.653201.

[2] S. Mahapatra *et al.*, "A comparative study of different physics based NBTI models," *IEEE Trans. Electron Devices*, vol. 60, no. 3. pp. 901–916, Mar. 2013.

[3] G. Rzepa *et al*, "Comphy — A compact-physics framework for unified modeling of BTI", *Microelectronics Reliability*, vol. 85, pp. 49-65, 2018. doi: 10.1016/j.microrel.2018.04.002

[4] J. H. Stathis *et al*, "Controversial issues in negative bias temperature instability," *Microelectronics Reliability*, vol. 81, pp. 244–251, Feb. 2018. doi: 10.1016/j.microrel.2017.12.035.

[5] S. Mukhopadhyay *et al*, "A Comprehensive DC and AC PBTI Modeling Framework for HKMG n-MOSFETs", *IEEE Trans. Electron Devices*, vol. 64, no. 4. pp. 1474–1484, April. 2017.

[6] N. Parihar, N. Goel, S. Mukhopadhyay, and S. Mahapatra, "BTI analysis tool-modeling of NBTI DC, AC stress and recovery time kinetics, nitrogen impact, and EOL estimation," *IEEE Trans. Electron Devices*, vol. 65, no. 2, pp. 392–403, Feb. 2018. doi: 10.1109/TED.2017.2780083.

[7] S. Mahapatra, N. Parihar, "Modeling of NBTI Using BAT Framework: DC-AC Stress-Recovery Kinetics, Material, and Process Dependence", IEEE Trans. Device and Material Reliability, vol. 20, pp. 4-23, March 2020, doi: 10.1109/TDMR.2020.2967696.

[8] N. Chaudhary *et al*, "Analysis of The Hole Trapping Detrapping Component of NBTI Over Extended Temperature Range" in *Proc. IEEE Int. Rel. Phys. Symp. (IRPS), 2020*, doi: 10.1109/IRPS45951.2020.9129245.

[9] R. Tiwari *et al*, "A 3-D TCAD Framework for NBTI— Part I: Implementation Details and FinFET Channel Material Impact" *IEEE Trans. Electron Devices*, vol. 66, TED May 2019, doi: 10.1109/TED.2019.2906339.

[10] S. Mukhopadhyay *et al*, "Trap Generation in IL and HK Layers During BTI /TDDB Stress in Scaled HKMG N and P MOSFETs", in *Proc. IEEE Int. Rel. Phys. Symp. (IRPS), 2014*, doi: 10.1109/IRPS.2014.6861146.

[11] M. A. Alam *et al*, "Field acceleration for oxide breakdown-can an accurate anode hole injection model resolve the E vs. 1/E controversy? in *Proc. IEEE Int. Rel. Phys. Symp. (IRPS), 2000*, doi: 10.1109/RELPHY.2000.843886.

[12] *SentaurusTM Process User Guide*, document N-2017.09, 2017.

[13] *SentaurusTM Device user guide*, document N-2017.09, 2017.

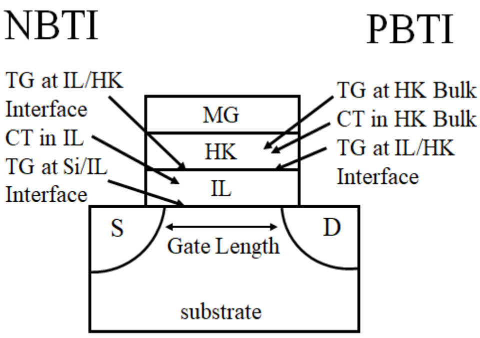

Fig.1. Schematic of the trap generation (TG) and trapping (CT) mechanism is shown under both NBTI and PBTI stress for a planar HKMG device.

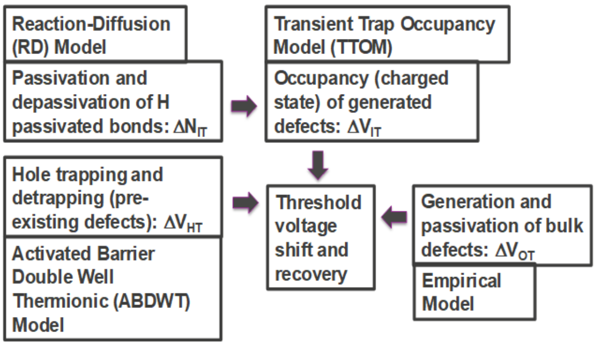

Fig.2. Schematic of BAT framework for both NBTI and PBTI stress-recovery for a planar HKMG device. ΔV_T subcomponents and corresponding models are shown.

$$K_{F1} \sim K_{F10} * \exp(-E_{AKF1}/kT) * \exp(\Gamma_E E_{ox})$$

$$K_{F10} \sim p_H T_H \sigma$$

$$T_H \sim \exp(-\sqrt{m_T \varphi_B})$$

$$\Gamma_E = \Gamma_0 + \alpha/kT$$

$$\Gamma_0 \sim \sqrt{\frac{m_T}{\varphi_B}}$$

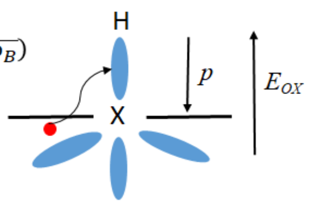

Fig.3. Schematic of H passivated bond dissociation process at the channel/IL interface used in CEDM [9].

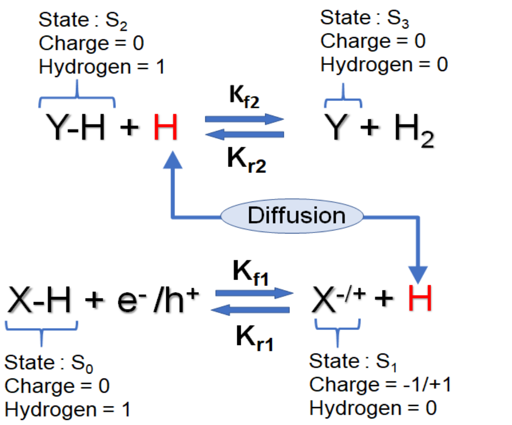

Fig.4. Multi State Configuration Model schematic, utilizing CEDM, showing Hydrogen Transport degradation mechanism at the two interfaces for N(h+) and P(e-) BTI.

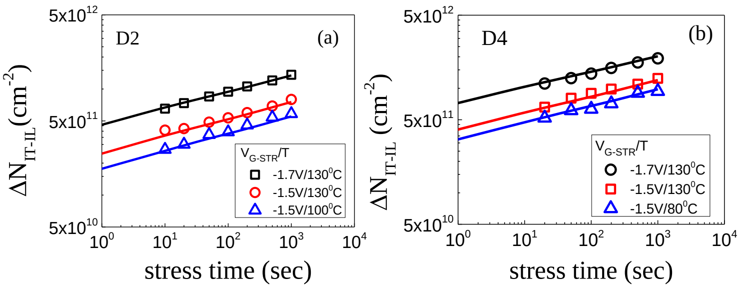

Fig.5. TCAD modeling of DCIV measured ΔN_{IT-IL} time kinetics showing increased NBTI degradation for (b) nitrided device (D4) as compared to (a) non-nitride device (D2). Lines: TCAD simulation, symbols: DCIV data.

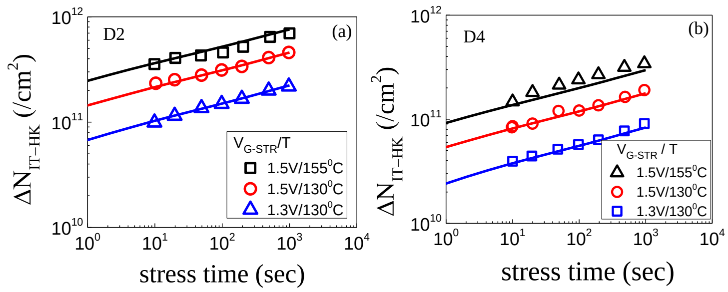

Fig.6. TCAD modeling of DCIV measured ΔN_{IT-HK} time kinetics showing lower PBTI degradation for (b) nitrided device (D4) as compared to (a) non-nitride device (D2). Lines: TCAD simulation, symbols: DCIV data.

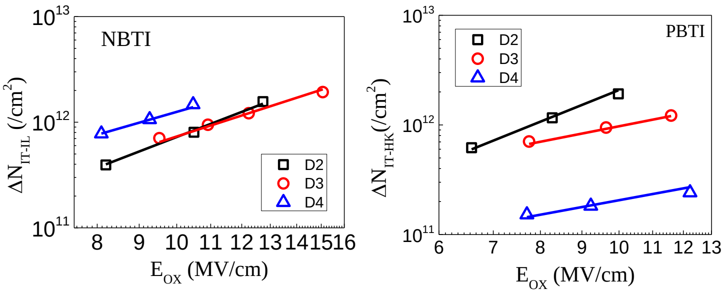

Fig.7. TCAD modeling of field dependence of DCIV measured ΔN_{IT-IL} for N (left), and ΔN_{IT-HK} P(right) BTI for different IL scaled devices. Lines: TCAD simulation, symbols: DCIV data.

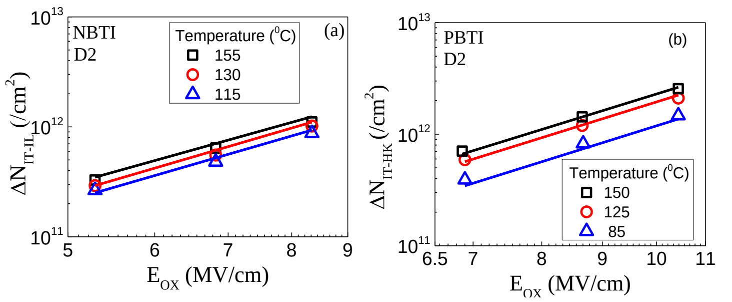

Fig.8. TCAD modeling of field dependence of DCIV measured TG, ΔN_{IT-IL} for (left) N and ΔN_{IT-HK} for (right) P BTI at different temperature. Lines: TCAD simulation, symbols: DCIV data.

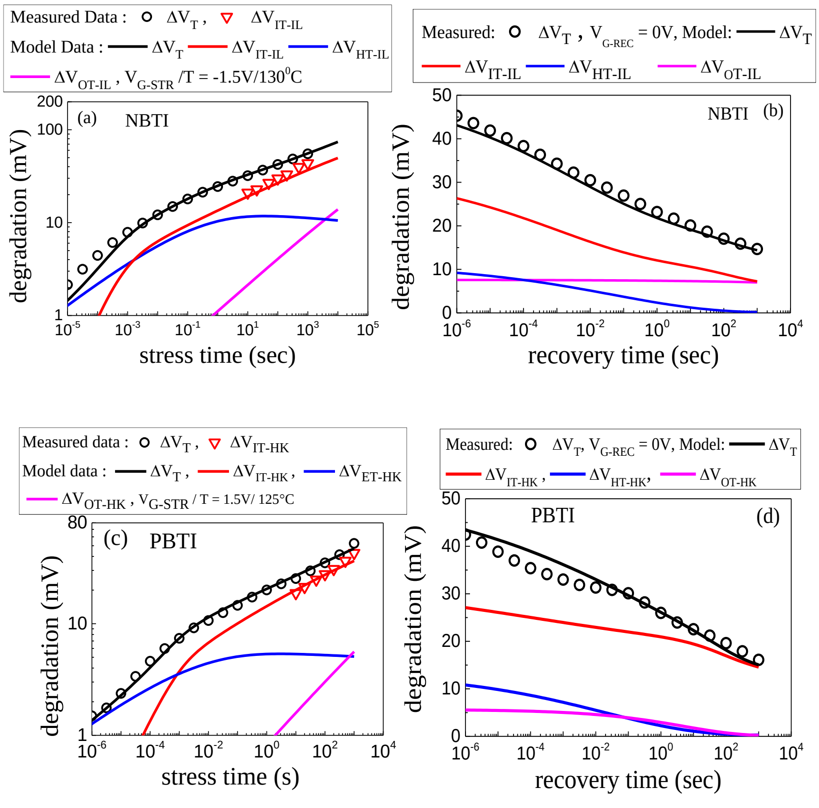

Fig.9. BAT modeling of ultra-fast measured ΔV_T and DCIV measured TG time kinetics for top: NBTI during (a) stress and (b) recovery; and bottom: PBTI during (c) stress and (d) recovery; at fixed $V_{G\text{-}STR}$-T and the sub-components are shown. Overall ΔV_T is dominated by ΔV_{IT} subcomponent.

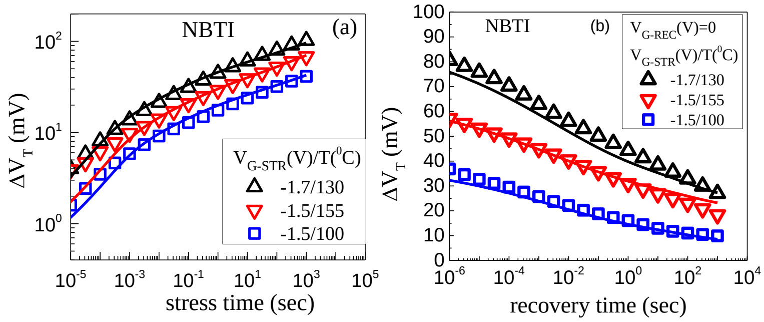

Fig.10. BAT modeling of ultra-fast measured NBTI ΔV_T time kinetics for (a) stress and (b) recovery at different $V_{G\text{-}STR}$-T are shown. Only few cases of $V_{G\text{-}STR}$-T are shown for better visibility. Measured data: symbols, model data: lines.

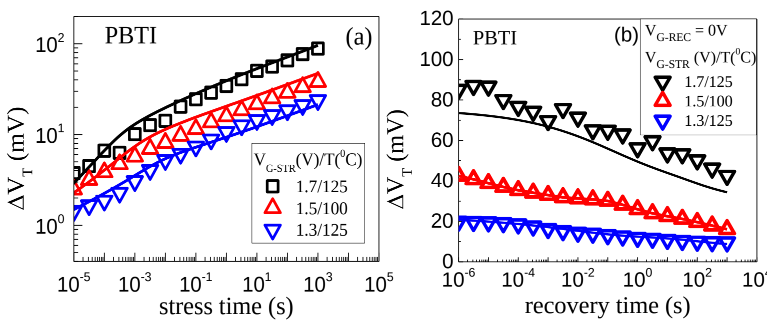

Fig.11. BAT modeling of ultra-fast measured NBTI ΔV_T time kinetics for (a) stress and (b) recovery at different $V_{G\text{-}STR}$-T are shown. Only few cases of $V_{G\text{-}STR}$-T are shown for better visibility. Measured data: symbols, model data: lines.

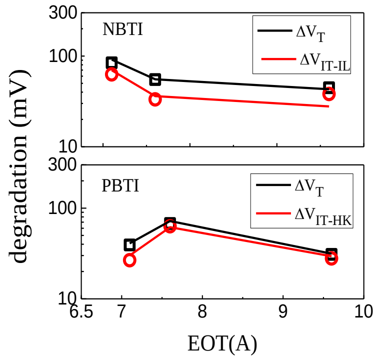

Fig.12. Ultra-fast measured fixed time ΔV_T and TG from DCIV, NBTI (top), and PBTI (bottom); for different IL-scaled devices are modeled using BAT. Measured data: symbols, model data: lines.

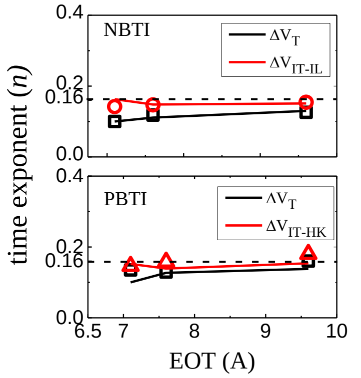

Fig.13. Time slope of ultra-fast measured ΔV_T and TG from DCIV, NBTI (top), and PBTI (bottom); for different IL-scaled devices are modeled using BAT. Measured data: symbols, model data: lines.

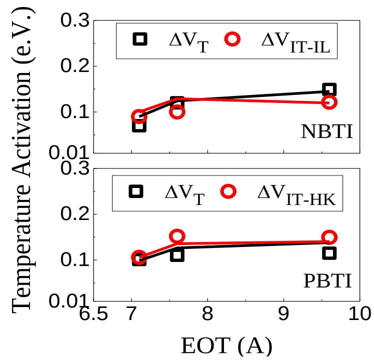

Fig.14. Temperature Activation Energy (E_A) of ultra-fast measured ΔV_T and TG from DCIV, NBTI (top), and PBTI (bottom); for different IL-scaled devices are modeled using BAT. Measured data: symbols, model data: lines.

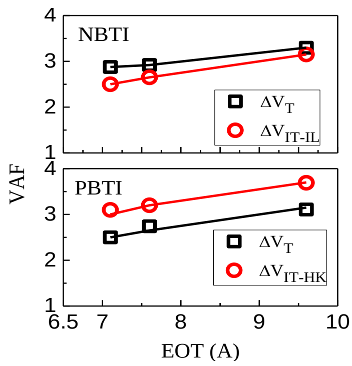

Fig.15. Voltage Acceleration Factor (VAF) of ultra-fast measured ΔV_T and TG from DCIV, NBTI (top), and PBTI (bottom); for different IL-scaled devices are modeled using BAT. Measured data: symbols, model data: lines.